RSC Advances

PAPER

View Article Online
View Journal | View Issue

Cite this: *RSC Adv.*, 2020, **10**, 20349

A stable and highly sensitive room-temperature liquefied petroleum gas sensor based on nano-cubes/cuboids of zinc antimonate

Satyendra Singh, *[a] Archana Singh,[b] Ajendra Singh[b] and Poonam Tandon *[b]

Received 6th March 2020
Accepted 5th May 2020

DOI: 10.1039/d0ra02125c

rsc.li/rsc-advances

Trirutile zinc antimonate ($ZnSb_2O_6$) nano-cubes/cuboids have been fabricated by a sol–gel spin-coating method using polyethylene glycol (PEG) as the structure-directing agent. The fabricated films were characterized for surface morphology, along with structural, FT-IR and thermal analysis. The crystallite size of $ZnSb_2O_6$ is found to be 35 nm. The fabricated films have been tested for the detection of liquefied petroleum gas (LPG) and carbon dioxide (CO_2) gas leakage at room temperature (27 °C). They exhibit fairly high sensitivity (1.73), low response and recovery times (~41 and 95 s, respectively), and good reproducibility and stability (99.2%) at room temperature for the detection of LPG leakage. Based on these observations, the fabricated film has the potential to be used as a LPG sensor at room temperature.

Introduction

A gas sensor is a device that creates an electrical or optical signal in response to chemical interaction with gases and thus detects the presence of harmful gases. The development of gas sensors, especially liquefied petroleum gas (LPG) sensors, is of prime importance for the safely requirements in homes, hotels, industries, offices associated with kitchens, and others. The LPG sensor presents an alarm upon the leakage of LPG. The leakage of LPG may be due to mistakes or accidents, and may take the form of explosion accidents. A reliable and sensitive LPG sensor presents an alarm for the leakage of LPG and thus increases our safety. Therefore, in recent years, LPG sensing has motivated intense research activities across the world for the development of new sensing materials and technologies, in view of fundamental research as well as industrial applications.[1–5] Most of the LPG sensors reported in the open literature basically work at very high operating temperatures, such as 250 °C or above, which is not facile for commercialization of the sensor.[1,3–8] Therefore, nowadays, the sensor community is focusing on the development of a potential LPG sensor operable at room temperature and that produces a quick response, *i.e.*, small response and recovery times towards the incoming LPG, along with high sensitivity, reproducibility and stability.[9–13] The sensing mechanism of such LPG sensor is a surface-controlled phenomenon; therefore, nanostructures play a significant role for the design of sensing devices. Hence, for the sensor community, the correlation between structure and sensing properties is an active area of sensor research and development.[14–22]

Nanostructured semiconducting oxides that possess porous surfaces are being used in the construction of gas sensors. Most of the sensing assessments of nanostructured semiconducting materials are based on the surface morphology, such as nanospheres, nanorods, nanonails, nanobeads, nanodisks, nanocones, nanospindles, nanoflowers, nanowires, hollow and solid spheres, tetrapods *etc.*[2,4,12–23] On the other hand, in this work, the sensing properties were investigated by fabricating a nanocube/cuboid-structured surface morphology for a new LPG-sensitive material at room temperature. Thus, the present study reports the gas-sensing properties of a different kind of surface morphology of nanostructured zinc antimonate. In order to modify the electrical/sensing properties of nanostructured metal oxides, their size and shape should be controlled by various capping agents, such as surfactants, ligands and polymers. These capping agents confine the growth of the metal oxide to the nanoscale region. In most cases, these methods produce spherical particles due to their low surface energy; however, in some cases, other shapes are also formed.[5,17,20] Such structural diversity can be achieved as a result of specific interactions of the structure-directing agent with different growth faces of the particles.[24]

Nanostructured SnO_2, which possesses the rutile-type structure, is one of the most studied gas-sensing materials.[25–32] Rutile is a well-known inorganic structure that has been investigated for several applications, including sensors.[25–32] However, in the case of trirutile-type structure (such as $MgSb_2O_6$, $ZnSb_2O_6$, $CoSb_2O_6$, $CuSb_2O_6$, $NiSb_2O_6$, $MnSb_2O_6$, *etc.*), few studies have been reported on the gas-sensing properties.[33–42] Nanostructured trirutile-type materials have also been reported for their photocatalytic activity and for their

[a]*Department of Physics, M.P. Govt. P.G. College, Hardoi 241001, U.P., India. E-mail: satyendra_nano84@rediffmail.com*

[b]*Macromolecular Research Laboratory, Department of Physics, University of Lucknow, Lucknow-226007, U.P., India. E-mail: poonam_tandon@yahoo.co.uk*

supercapacitor, energy and environmental applications, as well as in Li-ion batteries *etc.*[43–52] The sensing properties of antimonate/trirutile-based gas sensors are summarized in Table 1. Moreover, there are no reports on the LPG sensing of trirutile-based gas sensors.[33–42] From Table 1, it is noticeable that the sensors based on these materials are reported at high operating temperatures that require additional power consumption. In fact, these sensors have a decreased sensor stability due to the high temperature of operation, which is inconvenient for the fabrication of a sensor device. In particular, Bonilla *et al.*[34] have synthesized zinc antimonate by a microwave-assisted solution method. They investigated the CO and C_3H_8 sensitivity behaviour of zinc antimonate at 150–250 °C temperature range. At ambient temperature (23 °C), no variation of the sensitivity was observed. The maximum value of sensitivity they detected was 1.26 for a propane concentration of 300 ppm, at an operating temperature of 250 °C. However, in the present investigation, an attempt has been made to develop an efficient LPG sensor operable at room temperature, as the sensing of LPG at room temperature plays an important role for its commercialization. In addition, room-temperature operation of a sensor increases its lifetime and stability. Thus, LPG sensors operable at room temperature are in high demand for both domestic and industrial purposes.

Goutham *et al.*[53] have fabricated a LPG sensor at room temperature (27 °C) based on a CdO/graphene nanocomposite. They studied the sensor properties of CdO and CdO/graphene (1, 2 and 3 wt%) nanocomposite at various operating temperatures, from 27 °C to 225 °C, and LPG concentrations between 100 ppm to 800 ppm. They reported a maximum response of 0.77 for 600 ppm of LPG at an operating temperature of 27 °C. Ghule *et al.*[54] reported the room-temperature LPG sensitivity of graphene oxide (GO), Fe_2O_3 and GO–Fe_2O_3 composite sensors. The maximum sensitivity they reported was 0.35 for the 1 wt% GO–Fe_2O_3 composite sensor, obtained for 100 ppm of LPG at 27 °C. Thakur *et al.*[55] reported that poly(*o*-anisidine)-cerium oxide nanocomposite exhibits the sensitivity of 0.02 upon exposure to 900 ppm of LPG at room temperature. A room-temperature LPG sensor based on zinc oxide/polypyrrole/lead sulfide quantum dots nanocomposite film was fabricated by Zhang *et al.*[56] The value of maximum sensitivity they reported was 0.45 at 1000 ppm of LPG. A room-temperature LPG sensor based on α-Fe_2O_3/carbon nanotube nanocomposite films was reported by Chaitongrat *et al.*[57] Their sensor demonstrates a sensitivity of 0.05 for 7000 ppm of LPG. Saxena *et al.*[58] demonstrated a room-temperature LPG sensor by employing CdS : SiO_2 nanocomposite thin films. The highest sensitivity observed was 0.71 for 1000 ppm of LPG at room temperature, with the response and recovery times of 91 and 140 s, respectively. Thus, the maximum sensitivity of room-temperature LPG sensor reported in the literature is 0.77 for 600 ppm of LPG, as investigated by Goutham *et al.*[53]

Nanostructured trirutile oxides based on antimony show very good surface reactivity due to the fact that antimony acts as a catalyst.[43–47] They show remarkable catalytic properties in oxidation reactions due to the high oxygen ion mobility at the film surface and, thus, are highly interesting for the development of a gas sensor.[43–47] Noble metal catalysts such as antimony, when coated on the oxide surface, result in improvement of the sensing capabilities, as antimony tends to promote chemical reactions by reducing the activation energy between the oxide and the gas to be detected.[59] Therefore, antimony-based trirutile nanostructured oxide materials (antimonates) are promising, as they increase the rate of reaction (adsorption/desorption) between the incoming target gas molecules and the sensing layers.[40] This is quite significant to improve the sensitivity, selectivity, repeatability, stability, and response and recovery times of the sensor. Antimony acts as a catalyst for the dissociation of oxygen over the film surface and, thus, enhances the spillover of oxygen species over the film surface, which may enhance the sensitivity of the sensor.[59] The increased reactivity of nanostructured antimonates at room temperature may result in an increase in the sensitivity, which diminishes the required power consumption and, thus, has a valuable effect on the stability and lifetime of the sensor. Therefore, the primary objective of our research is to synthesize nanostructured antimonate material suitable for the development of a gas sensor.

Table 1 The sensing responses of earlier reported antimonate-based gas sensors

Sl. No.	Sensing material	Target gas	Conc. of gas	Operating temperature	Sensor response	Reference
1	Manganese antimonate	CO	300 ppm	200 °C	0.33	37
2	Manganese antimonate	CO	300 ppm	300 °C	8.98	37
3	Manganese antimonate	Propane	500 ppm	200 °C	0.31	37
4	Manganese antimonate	Propane	500 ppm	300 °C	0.44	37
5	$CoSb_2O_6$ nanoparticles	CO	200 ppm	350 °C	7.00	39
6	$CoSb_2O_6$ nanoparticles	C_3H_8	300 ppm	350 °C	4.80	39
7	$NiSb_2O_6$ nanoparticles	C_3H_8	500 ppm	300 °C	1.10	41
8	$NiSb_2O_6$ nanoparticles	CO	300 ppm	300 °C	2.10	41
9	$MgSb_2O_6$ nanorods	CO	300 ppm	200 °C	3.87	42
10	$MgSb_2O_6$ nanorods	C_3H_8	300 ppm	250 °C	47.62	42
11	$ZnSb_2O_6$ micro-wires/rods	C_3H_8	300 ppm	250 °C	1.26	34
12	$ZnSb_2O_6$ micro-wires/rods	CO	300 ppm	250 °C	6.66	34
13	$ZnSb_2O_6$ nano-cubes/cuboids	CO_2	5000 ppm	27 °C	1.46	Present work
14	$ZnSb_2O_6$ nano-cubes/cuboids	LPG	5000 ppm	27 °C	1.73	Present work

In this work, we demonstrate an efficient approach for the synthesis of nanocrystalline cubes/cuboids of $ZnSb_2O_6$ *via* sol–gel method using PEG as a structure-directing agent. Further, the main focus was on the characterization and investigation of sensing performance at room temperature (27 °C). The sensitivity of the $ZnSb_2O_6$ sensor was studied by measuring the electrical resistance of the sensor in air and in a reducing gas environment (LPG), as well as in an oxidizing gas environment (CO_2). This approach is useful for the development of trirutile nanostructured antimonate and provides an effective way to examine the influence of surface morphology on the gas-sensing properties. The utilization of nanostructured zinc antimonate is a relatively new approach towards LPG sensing at room temperature.

Experimental

Synthesis and growth mechanism of nano-cubes/cuboids of $ZnSb_2O_6$

Sol–gel method was used for the synthesis of nanocrystalline zinc antimonate ($ZnSb_2O_6$). The stoichiometric amount of starting materials, such as zinc sulphate ($ZnSO_4 \cdot 7H_2O$) and antimony trichloride ($SbCl_3$), were taken and dissolved in the required amount of ethanol to prepare 0.1 M solution of each precursor. Both precursors (zinc and antimony) were then mixed with each other and magnetically stirred at 80 °C for 2 h with drop-by-drop addition of 20 mL polyethylene glycol (PEG). Thus, the gel of zinc antimony oxide was formed. This gel was used for the fabrication of thin films for sensing purposes. PEG works as a structure-inducing capping agent and controls the growth rate during the precipitation process.[60] Further, ammonium hydroxide solution was added drop by drop to the above mixed solution, and a white colour precipitate was obtained. This reaction was carried out at pH ~ 8. Further, this solution was stirred at 80 °C for 6 h. The resulting precipitate was annealed at 600 °C for 2 h. Afterwards, the crystalline powder was crushed into fine powder.

Thin films of the precursor were fabricated on alumina substrate (10 × 10 mm^2) using a spin coater (Metrex Scientific Instruments, India) at 2000 rpm for 60 s. The fabricated films were dried at 80 °C for 6 h and then annealed at 600 °C for 2 h for the proper stabilization of the films. The annealing of sensing films at high temperature has been reported by several researchers to achieve long-term stability, high sensor response and short response and recovery times.[5,7,37–39] During thermal treatment, the oxygen species are adsorbed in the forms O_2^-, O^- and O^{2-} on surface of thin films, which are highly reactive towards the incoming gas molecules. Therefore, these oxygen species play a significant role in the gas-sensing phenomenon.[5,7,37–39] When the fabricated thin film is annealed and stabilized, the sensor surface possesses nano-cube/cuboid-structured surface morphology. The thickness of the film was found 300 nm, measured by an Accurion variable angle spectroscopic ellipsometer (Nanofilm EP3 Imaging).

The mechanism of formation of nano-cubes/cuboids proceeds through successive nucleation and growth steps. In the synthesis of nano-cubes/cuboids of zinc antimonate, the basic principle for shape control involves two major steps: (i) the formation of spherical nanocrystallites, which grow by their linear arrangements into various shapes, such as tripods and tetrapods, *etc.*,[23] and (ii) the bending of primary nanocrystals at their edges to form various morphologies.[23] This is probably due to the presence of the structure-directing agent, polyethylene glycol (PEG). The proposed scheme for the growth of nano-cubes/cuboids of $ZnSb_2O_6$ is depicted in Scheme 1. In this scheme, the preliminary spherical nanocrystallites (in precursor solution) are formed due to their low surface energy. In the next stage, the spherical nanocrystallites are grown into the various intermediate shapes, such as tetra-pods, tri-pods and Y *etc.*[23] These nanocrystallites finally transform into nanocubes and nanocuboids of zinc antimonate.

Characterization techniques for nano-cubes/cuboids of $ZnSb_2O_6$

The synthesized material was characterized in structural investigations by X-ray diffractometer (X-Pert PRO PANalytical). The XRD data was recorded using Cu K_α radiation having a wavelength $\lambda = 1.5406$ Å. The crystallite size of $ZnSb_2O_6$ was calculated by Debye–Scherrer's equation. The surface morphologies of the sensing films were observed by scanning electron microscope (SEM-LEO). Optical characterizations were done by UV-visible absorption spectrophotometer (Varian, Carry-50 Bio) in UV and visible region and with a Fourier transform infrared spectrometer (Tensor-27). Differential scanning calorimeter (Mettler Toledo) was used for the thermal analysis of nanosized zinc antimony oxide.

Gas-sensing properties of nano-cubes/cuboids of $ZnSb_2O_6$

For the gas-sensing measurements, silver electrodes (ohmic contacts) were grown on two opposite ends of the film for the measurement of film resistance. Further, the fabricated sensing film was inserted inside the sensing chamber and stabilized in air for 10 to 15 min. This stabilized resistance is known as resistance in the presence of air (R_a). After stabilization of the film, a known concentration of target gas was passed inside the gas chamber, and the temporal variations in resistance of the films for different concentrations (1000 to 5000 ppm) of gas were recorded by a Keithley electrometer (Model 6514). The films were investigated by exposure to LPG and CO_2 at room temperature (27 °C). For this purpose, a special gas chamber was designed,[61,62] which consists of an inlet knob for target gas entry into the chamber, and an outlet knob for the removal of stored gas. The details of the gas-sensing setup are mentioned in our previous publications.[61,62]

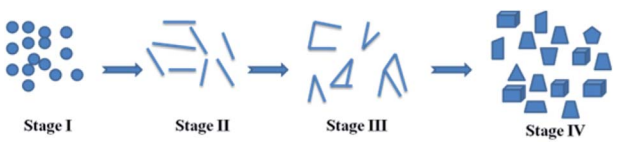

Scheme 1 The stages of growth of the nano-cubes/cuboids of $ZnSb_2O_6$.

The sensing parameters, *e.g.*, sensitivity/sensor response, reproducibility, stability, and response and recovery times, were calculated in order to analyze the observed sensing performance. These parameters are defined below:[63,64]

(i) Sensor response is defined as the relative change in resistance of the sensor with respect to stabilized resistance in air, and is given by the formula:[63,64]

$$\text{S.R.} = \frac{R \sim R_o}{R_o},$$

where R is the resistance of the sensor in the presence of target gas at any time t, whereas R_o is the stabilized resistance of the sensor in air.

(ii) Reproducibility is the repeatability of the sensing experiments, and reproducibility after long run of a sensor is known as stability of the sensor.

(iii) Response time is defined as time taken by the sensing material to acquire 90% of the maximum change in its resistance,[63,64] whereas recovery time is defined as the time taken by the sensor to reacquire 10% of the stabilized value of its initial resistance in the absence of gas.

Results and discussion

Surface morphology and structural analysis

The surface morphologies of nanocrystalline $ZnSb_2O_6$ film annealed at 600 °C are shown in Fig. 1(a) and (b). Herein, Fig. 1(a) is the surface morphology of the film sensor stabilized in air, and Fig. 1(b) is the surface morphology of the film sensor after exposure to LPG. In Fig. 1(a), most of the particles appear as nanocubes, whereas the rest are nanocuboid in shape, having sharp boundaries. Isolated particles (separate nano-cubes/cuboids) have been found over the entire surface of the film. This is due to the fact that during annealing, PEG is adsorbed and acts as a bridge between the particles. The linear chains of PEG can be cross-linked in aqueous medium (ethanol).[12] The cross-linking between the chains may provide small cages wherein the reactant mixture gets trapped. Further, during annealing at 600 °C, the reactant mixture trapped in the cages reduces to separate nano-cubes/cuboids. Thus, the cages formed by cross-linking may offer resistance to the agglomeration of the particles and yields separate nano-cubes/cuboids. The average size of nanocubes was found to be ~60 nm. The nano-cubes/cuboids of zinc antimonate become enlarged, with diffuse boundaries, when exposed to the gas, as seen in Fig. 1(b). These properties of nano-cubes/cuboids of zinc antimonate create an interesting possibility for implementation towards the development of LPG sensors operable at room temperature. Among the other features, the surface morphology has strong influence on both the sensitivity and the charge transfer process. In this paper, we have investigated the influence of surface morphology of the film (sensing layer) on its sensing properties. Microwires and microrods of zinc antimonate were prepared by Bonilla *et al.*[34] using the microwave-assisted solution method. The average length and diameter of microwires they reported are 59.5 μm and 1.5 μm, respectively. On the other hand, the $ZnSb_2O_6$ nano-cubes/cuboids we fabricated using the sol–gel spin-coating method have an average size of ~60 nm. Comparatively, we obtained better results here in terms of surface morphology.

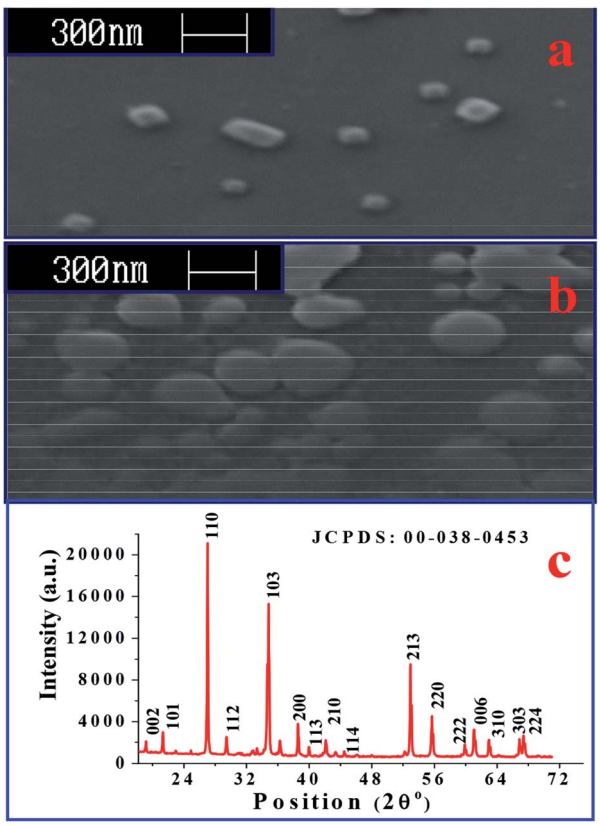

Fig. 1 SEM images of $ZnSb_2O_6$ (a) before exposure to LPG and (b) after exposure to LPG, and (c) the X-ray diffraction pattern of $ZnSb_2O_6$ annealed at 600 C°.

The XRD pattern of the synthesized material annealed at 600 °C is shown in Fig. 1(c). The [*h k l*] planes have been identified at each peak of the diffraction pattern. All XRD peaks belong to $ZnSb_2O_6$ (JCPDS: 00-038-0453) and are indexed accordingly. The average crystallite size has been found to be 35 nm using the Debye–Scherrer equation. In the previous report on the synthesis of $ZnSb_2O_6$ by Bonilla *et al.*,[34] a similar XRD pattern was reported. However, a secondary phase $ZnSb_2O_4$ was also observed in addition to $ZnSb_2O_6$ phase. On the other hand, we observed only $ZnSb_2O_6$ phase, which indicates that our synthesis approach is obviously better than earlier reported synthesis method[34] (microwave-assisted solution method).

Optical and thermal analysis

In order to understand the reaction process during synthesis of $ZnSb_2O_6$ associated with temperature, it was characterized by FT-IR. So as to observe the FT-IR spectra, transmittance of the synthesized $ZnSb_2O_6$ was recorded against wavenumbers in the region between 400 and 4000 cm^{-1}. Fig. 2(a) shows the FT-IR spectra of pre-(as synthesized) and post-annealed (annealed at 600 °C) nanostructured trirutile $ZnSb_2O_6$. The bands of the as-synthesized (pre-annealed) material have been observed at 493, 613, 836, 1159, 1392, 1616, 2365, 3124 and 3581 cm^{-1}. The

observed bands in the low-frequency region (493 and 613 cm^{-1}) are assigned as metal–oxygen (Zn–O and Sb–O modes) stretching vibrations, respectively. The additional observed vibration bands may be assigned to O–H stretching (broad absorption at 3581 cm^{-1}) and O–H bending vibration (1616 cm^{-1}; hydroxyl bands of adsorbed water). The peak at 1159 cm^{-1} is due to C–C stretching. The presence of FT-IR frequencies at low wavenumbers also provides evidence of Zn–Sb complex formed during continuous stirring. On the other hand, bands in the annealed material are observed at 493, 594, 633, 704, 1099, 2365 and 3559 cm^{-1}. Slight variations in peak position and intensity are observed for the peak at 3559 cm^{-1}. After annealing of the material at 600 °C, the peak intensity of this band decreases due to complete conversion of hydroxides into the corresponding oxide. The slight variations in peak position at low wavenumbers are due to the degradation of organic groups present in the precursor. Based on FT-IR analysis, the peak in the DSC curve at 147 °C may be due to the desorption of physisorbed water molecules.

Fig. 2(b) shows the variation in UV-visible absorption of $ZnSb_2O_6$ precursor for both as-synthesized and annealed materials in the 200–800 nm wavelength range. It is clear that the peak shifts to longer wavelengths on moving from precursor, to as-synthesized, to annealed materials, and their respective peaks were observed at 219, 271, and 274 nm. The absorption coefficient (α) is given by:

$$\alpha = 2.303\left(\frac{A_b}{t}\right)$$

In the above equation, A_b is the absorbance, and t is the thickness of the cuvette. The plot of $(\alpha h\nu)^2$ *vs.* $h\nu$ for the annealed $ZnSb_2O_6$ is shown in Fig. 2(c). From the figure, the energy band gap of $ZnSb_2O_6$ was found to be 3.65 eV.

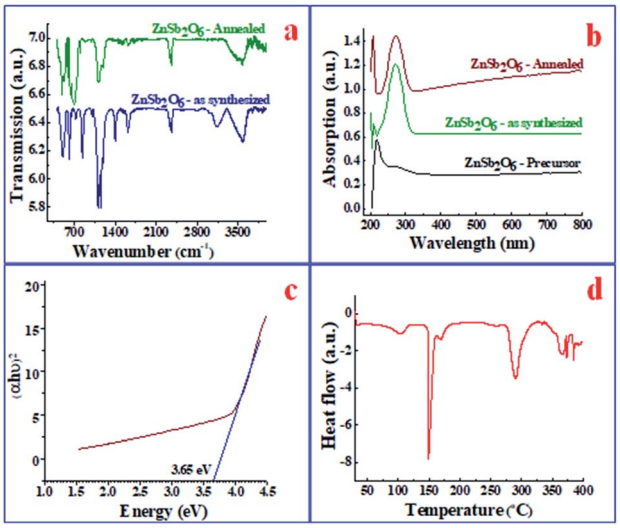

Fig. 2 (a) FTIR spectra of as-synthesized and annealed $ZnSb_2O_6$, (b) UV-visible spectra of the precursor, and as-synthesized and annealed $ZnSb_2O_6$, (c) Tauc plot for band gap calculations of annealed $ZnSb_2O_6$, and (d) the DSC curve of as-synthesized $ZnSb_2O_6$.

The DSC curve of the as-synthesized powder is presented in Fig. 2(d). The endothermic peaks at 103, 147, 169, 291 and 365 °C appearing in the DSC curve indicate the removal of chemical impurities, excess PEG and ammonium oxide, and the formation of zinc antimony hydroxide.

Gas-sensing analysis of the $ZnSb_2O_6$ film sensor

The aim of the present paper is to examine the gas-sensing properties of trirutile $ZnSb_2O_6$ film sensor with nano-cube/cuboid-structured surface morphology. To perform the sensing experiments, fabricated film was inserted inside the sensing chamber and stabilized in air for 10–15 min. This stabilized resistance is known as resistance in the presence of air (R_a). Further, a known concentration of target gas was passed inside the chamber, and the temporal variations in resistance for different concentrations of gas were observed. The film is investigated with exposure to CO_2 and LPG at room temperature, as discussed below.

CO_2-sensing performance of $ZnSb_2O_6$

The variations of electrical resistance ($\log R$) with time for different concentrations (1000–5000 ppm) of CO_2 are shown in Fig. 3(a). The observed variations of electrical resistance are divided in three regions, *i.e.*, stabilization process in air, response characteristics, and recovery characteristics. In region I, *i.e.*, in the stabilization process, the resistance decreases in beginning, and afterwards, it becomes saturated in air (R_a). Once the resistance becomes saturated, CO_2 is passed in the sensing chamber to detect the response characteristics of the sensor. In the response characteristics (*i.e.*, in region II), each curve shows that as time increases, the resistance of the sensing film increases sharply in the beginning, and afterwards increases slowly, then becomes saturated. Finally, in order to study the recovery characteristics, on opening the outlet of the chamber, the resistance of the film decreases sharply and then slowly until it attains the stabilized value of resistance in air (R_a) for a further range of time. Fig. 3(b) exhibits the CO_2 sensitivity curves of the $ZnSb_2O_6$ film sensor. The maximum value of the sensitivity of the film sensor was 1.46, observed for 5000 ppm of CO_2. The response and recovery times were ~44 and 156 s, respectively, for 5000 ppm of CO_2. Reproducibility curves for the sensing of the $ZnSb_2O_6$ film sensor are shown in Fig. 3(c), which demonstrate the sensing characteristics are 96% reproducible after three months of fabrication of the sensor, indicating the high stability and reproducibility of the gas-sensing process. Some researchers have already investigated the CO_2-sensing properties of nanostructured materials at high operating temperatures (above 200 °C),[65–71] which is not convenient, as sensors operable at high temperatures require more power consumption than the sensors operable at room temperature. N. B. Tanvir *et al.*[72] reported the investigation of CO_2 reaction with copper oxide nanoparticles, which is room-temperature gas sensing. The reported sensing mechanism by Tanvir *et al.*[72] is based on the change in work function after exposure to the gas, without measurements of the response and recovery times of the sensor. However, in our investigation, the

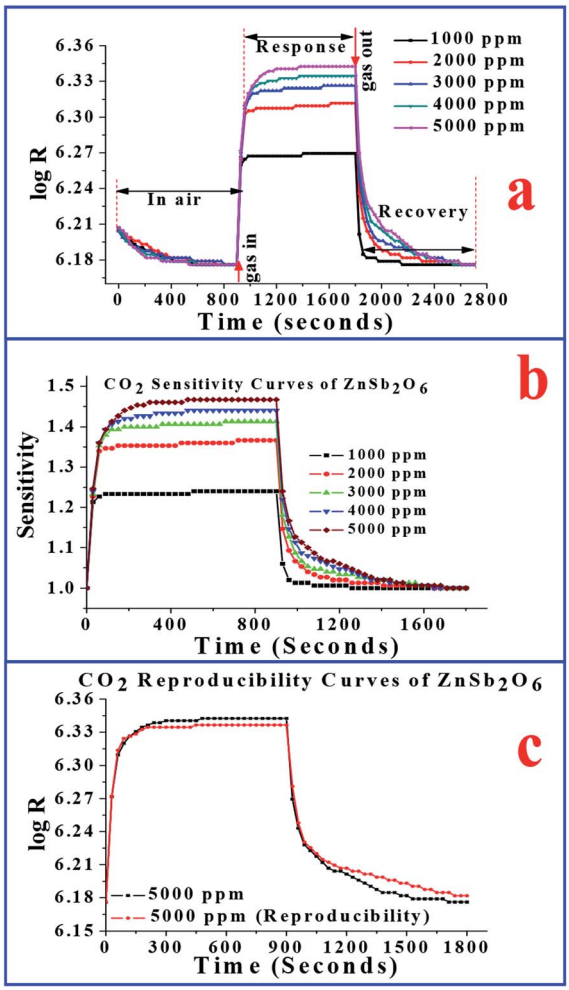

Fig. 3 (a) Variations in resistance (log R) with time for different concentrations of CO_2, (b) sensitivity curves of $ZnSb_2O_6$ for different concentrations of CO_2, and (c) reproducibility curves of $ZnSb_2O_6$ for 5000 ppm CO_2 three months after the fabrication of the sensor.

response of the sensor is based on the change in electrical resistance of the gas-sensitive layers, with the measurements of response and recovery times of the sensor.

LPG sensing performance of the $ZnSb_2O_6$ film sensor

The response of electrical resistance (log R) with time towards different concentrations of LPG (1000–5000 ppm) at room temperature is shown in Fig. 4(a). To explain the response of the sensor, this figure is divided into three regions (stabilization process in air, response characteristics, and recovery characteristics). In the process of stabilization, the film was inserted in the gas chamber, and variations in electrical resistance were observed as shown in region I. The resistance increases slowly in this region, and later on, it becomes saturated. Further, upon attaining the saturated value of resistance, response characteristics were observed upon exposure to different concentrations of LPG. Finally, recovery characteristics were observed on opening the chamber outlet. It is clear that the sensing response of the film increases with increasing concentration of LPG and

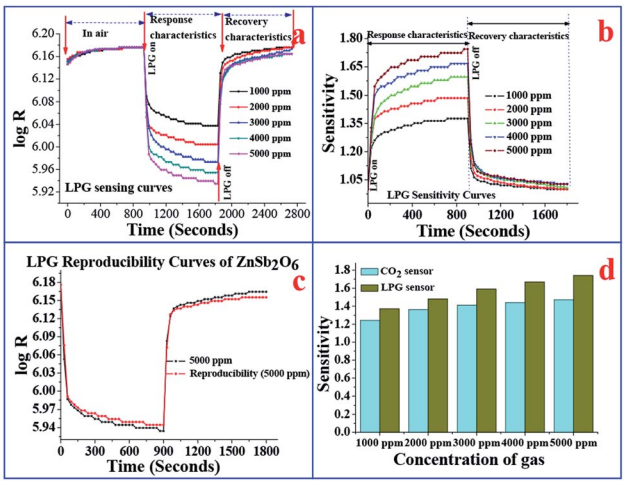

Fig. 4 (a) Variations in resistance with time for different concentrations of LPG, (b) sensitivity curves of $ZnSb_2O_6$ for different concentrations of LPG, (c) reproducibility curve of $ZnSb_2O_6$ for 5000 ppm LPG, and (d) comparison of sensitivities of the sensor for each concentration of CO_2 and LPG.

reaches a maximum at 5000 ppm of LPG. Sensitivity curves are shown in Fig. 4(b). We observe from this figure that the sensor possesses the maximum sensitivity of 1.73, which is larger than that for the CO_2 gas sensor. The $ZnSb_2O_6$ sensor exhibits response and recovery times of ~41 and 95 s, respectively, at room temperature for 1000 ppm of LPG. The recovery time is quite large in comparison to the response time due to the slow desorption of LPG at room temperature. The stability properties of the sensor have also been investigated and are shown in Fig. 4(c). The sensor shows sustainable behaviour (99.2% reproducible) even 3 months after fabrication of the sensor. The sensitivities of the sensor for LPG and CO_2 gas concentrations are plotted in Fig. 4(d). It is clear from the figure that sensor is more sensitive to LPG than CO_2 at each concentration.

From the above discussion, it is clear that the fabricated sensor is more sensitive towards LPG. Therefore, LPG sensing properties were investigated in more detail. The variations in resistance (log R) with time for four repeated exposure cycles of LPG are shown in Fig. 5(a). These multiple resistance switching cycles are plotted for 1000 ppm of LPG. Fig. 5(b) presents the response and recovery times of the sensor for different concentrations of LPG. Initially, the response time increases with LPG concentration up to 3000 ppm, and finally, it becomes saturated. However, the recovery time increases continuously with an increase in concentration of LPG. This may be due to the slow desorption rate of LPG at room temperature. As a result, high concentrations of LPG adsorption require a long time for complete desorption. Sensitivity of the LPG sensor as fabricated and after 2 months of fabrication against different concentrations of LPG is shown by Fig. 5(c), which obviously demonstrates the impressive reproducibility of the sensor. Fig. 5(d) reveals stability curves for the sensor of up to 60 days in a regular interval (every 6 days) of time for 1000 and 2000 ppm of LPG. From the figure, we observe that the sensor is 99%

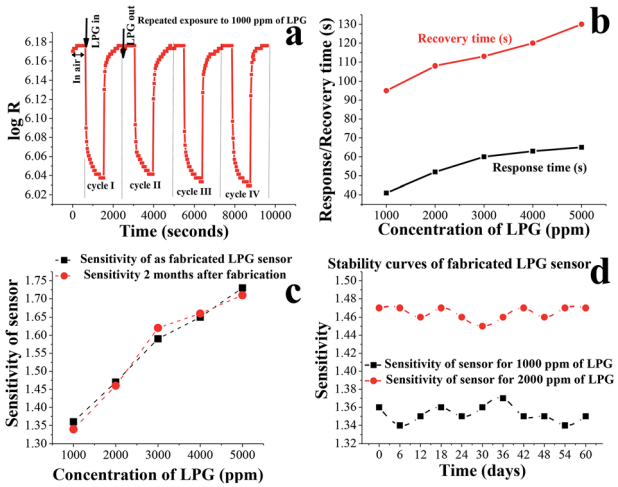

Fig. 5 (a) Variations in resistance with time for repeated exposure (cycles I–IV) to LPG, (b) response and recovery times with different LPG concentrations, (c) sensitivity of the LPG sensor, as fabricated and 2 months after fabrication, against different concentrations of LPG, and (d) stability curves of sensor for 1000 and 2000 ppm LPG.

stable for 1000 ppm of LPG, while its stability is 99.4% for 2000 ppm of LPG. Thus, our fabricated sensor possesses highly sensitive and long-term stability properties at room temperature. During the aging of the gas-sensitive nano-cube/cuboid layers, oxygen is diffused through both the macroporous (corresponding to molecular diffusion) and mesoporous (corresponding to Knudsen diffusion) regions, and these regions are charge depleted due to the chemisorption of oxygen. Therefore, the results concerning long-term stability over time present the sensor's suitability towards indoor gas-sensing applications. Moreover, we have already demonstrated that nano-cubes/cuboids are highly sensitive towards LPG. As a result, the fabricated sensor may be implemented for the leakage detection of LPG at room temperature.

The sensitivity of a sensor is mainly determined by the interactions between the target gas and the surface of a sensor. During LPG sensing, the LPG diffuses through macroporous and mesoporous regions and reacts with the chemisorbed oxygen. The diffusion of gases through the macroporous and mesoporous regions is known to play an important role in the sensing phenomenon.[63] Thus, as LPG comes into contact and reacts with the surface-adsorbed oxygen species (O_2, or O_2^-), more electrons are released back into the conduction band of $ZnSb_2O_6$, leading to a greater change of electrical resistance and, thus, increasing the sensitivity of the sensor. The possible interaction mechanism between adsorbed oxygen and $ZnSb_2O_6$ film surface may be seen in Fig. 6. In brief, atmospheric oxygen (O_2) is adsorbed on the film surface and extracts electrons from the conduction band of $ZnSb_2O_6$ to form oxygen species (O_2, or O_2^-) at room temperature.[63] These oxygen species react with alkanes of LPG, and electrons are released back into the conduction band of $ZnSb_2O_6$; thereby, resistance decreases upon exposure to LPG. In fact, the chemical reaction of the gas-

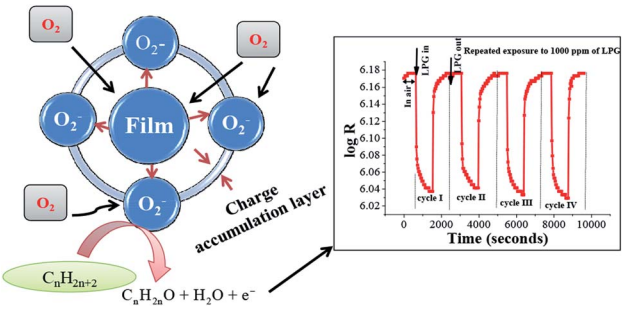

Fig. 6 Schematic diagram showing the interaction between oxygen and $ZnSb_2O_6$ and the corresponding resistance *versus* time graph for different exposure cycles of LPG.

sensitive layer with the incoming (target) gas results in the gas-detecting signal.

LPG sensors based on nanospheres, nanorods, nanoflowers, nanoellipses, nanonails, and vertical and horizontal rods have already been investigated,[1–13,40,59,61,64] but their sensing behaviours were found cumbersome to use due to their large response time. We have removed the above drawback of the sensor and fabricated nano-cube/cuboid-based LPG sensors with a short response time as compared to previous sensors reported in literature.[1–13,40,59,61,64] As discussed in introduction section, the maximum sensitivity of room-temperature LPG sensors reported in literature is 0.77 for 600 ppm of LPG, as investigated by Goutham *et al.*[53] However, the sensor we developed has a sensitivity of 1.36 for 1000 ppm of LPG, which is quite high in comparison to previous sensors reported below the lower explosive limit (LEL) of LPG. Moreover, the response and recovery times of our sensor are ~41 and 95 s, respectively, which are less than those observed by Saxena *et al.*[58] Therefore, in fact, our study is an advanced step towards the development of an efficient sensor for LPG detection. We believe that these findings not only render a novel synthesis of zinc antimonate nano-cubes/cuboids, but also provide nanostructured zinc antimonate for the fabrication of a gas sensor for the detection of LPG leakage with high response at room temperature.

Conclusions

$ZnSb_2O_6$ thin films were successfully fabricated and characterized for LPG and CO_2 sensing capabilities at 27 °C. SEM images reveal the nano-cube/cuboid-structured surface morphology of the films. X-ray diffraction confirms the formation of the $ZnSb_2O_6$ phase. The maximum sensitivity (1.73) of the sensor at room temperature was observed for 5000 ppm LPG, with response and recovery times of ~41 and 95 s, respectively. Moreover, the LPG sensor presents impressive long-term stability (99.2% reproducible) over a measurement period of 3 months, which plays a vital role towards the commercialization of the sensor. Finally, the room-temperature (27 °C) operation of the present sensor ensures its long-term stability. Therefore, the fabricated sensor has prospective use for LPG leakage detection at room temperature.

Conflicts of interest

There are no conflicts to declare.

Acknowledgements

The authors are thankful to Prof. Dr B.C. Yadav, Department of Applied Physics, Babasaheb Bhimrao Ambedkar University, Lucknow for fruitful discussion.

References

1 L. Satyanarayana, K. M. Reddy and S. V. Manorama, *Mater. Chem. Phys.*, 2003, **82**, 21–26.
2 B. C. Yadav, S. Singh and A. Yadav, *Appl. Surf. Sci.*, 2011, **257**, 1960–1966.
3 V. R. Shinde, T. P. Gujar, C. D. Lokhande, R. S. Mane and S. H. Han, *Sens. Actuators, B*, 2007, **123**, 882–887.
4 R. R. Salunkhe, D. S. Dhawale, U. M. Patil and C. D. Lokhande, *Sens. Actuators, B*, 2009, **136**, 39–44.
5 J. Y. Patil, M. S. Khandekar, I. S. Mulla and S. S. Suryavanshi, *Curr. Appl. Phys.*, 2012, **12**, 319–324.
6 K. V. Gurav, U. M. Patil, S. W. Shin, S. M. Pawar, J. H. Kim and C. D. Lokhande, *J. Alloys Compd.*, 2012, **525**, 1–7.
7 V. Hieu, L. T. N. Loan, N. D. Khoang, N. T. Minh, D. T. Viet, D. C. Minh, T. Trung and N. D. Chien, *Curr. Appl. Phys.*, 2010, **10**, 636–641.
8 S. Ray, P. S. Gupta and G. Singh, *J. Alloys Compd.*, 2010, **500**, 49–55.
9 R. B. Kamble and V. L. Mathe, *Sens. Actuators, B*, 2008, **131**, 205–209.
10 B. C. Yadav, A. Yadav, T. Shukla and S. Singh, *Sens. Lett.*, 2009, **7**, 1119–1123.
11 A. Singh, S. Singh, B. D. Joshi, A. Shukla, B. C. Yadav and P. Tandon, *Mater. Sci. Semicond. Process.*, 2014, **27**, 934–950.
12 A. S. Singh, S. Singh, B. C. Yadav and P. Tandon, *J. Alloys Compd.*, 2015, **618**, 475–483.
13 S. Singh, A. Singh, R. R. Yadav and P. Tandon, *Mater. Lett.*, 2014, **131**, 31–34.
14 C. Kuang, W. Zeng, H. Ye and Y. Li, *Physica E*, 2018, **97**, 314–316.
15 S. Hussain, T. Liu, M. Kashif, S. Cao, W. Zeng, S. Xu, K. Naseer and U. Hashim, *Mater. Lett.*, 2014, **128**, 35–38.
16 O. Lupan, V. Postica, V. Cretu, N. Wolff, V. Duppel, L. Kienle and R. Adelung, *Phys. Status Solidi*, 2016, **10**, 260–266.
17 D. Gedamu, I. Paulowicz, S. Kaps, O. Lupan, S. Wille, G. Haidarschin and Y. K. Mishra, *Adv. Mater.*, 2014, **26**, 1541–1550.
18 S. Hussain, T. Liu, M. S. Javed, N. Aslam and W. Zeng, *Sens. Actuators, B*, 2017, **239**, 1243–1250.
19 S. Hussain, T. Liu, M. Kashif, B. Miao, L. Lin, W. Zeng, M. Rashad, X. Peng and F. Pan, *J. Mater. Sci.: Mater. Electron.*, 2014, **25**, 4725–4729.
20 R. C. Pawar, J. S. Shaikh, S. S. Suryavanshi and P. S. Patil, *Curr. Appl. Phys.*, 2012, **12**, 778–783.
21 L. Zhu, W. Zeng, Y. Li and J. Yang, *Physica E*, 2019, **106**, 170–175.
22 Q. Guo, Y. Li and Z. Wen, *Physica E*, 2019, **114**, 113564.
23 V. Postica, J. Grottrup, R. Adelung, O. Lupan, A. K. Mishra, N. H. de Leeuw, *et al.*, *Adv. Funct. Mater.*, 2016, **27**, 1604676–1604690.
24 T. S. Ahmadi, Z. L. Wang, T. C. Green, A. Henglein and M. A. El-Sayed, *Science*, 1996, **272**, 1924–1926.
25 D. Haridas, K. Sreenivas and V. Gupta, *Sens. Actuators, B*, 2008, **119**, 270–275.
26 A. R. Babar, S. S. Shinde, A. V. Moholkar, C. H. Bhosale, J. H. Kim and K. Y. Rajpure, *J. Alloys Compd.*, 2011, **509**, 3108–3115.
27 B. Thomas, S. Benoy and K. K. Radh, *Sens. Actuators, B*, 2008, **133**, 404–413.
28 A. Sharma, M. Tomar and V. Gupta, *Sens. Actuators, B*, 2011, **156**, 747–752.
29 R. G. Deshmukh, S. S. Badadhe, M. V. Vaishampayan and I. S. Mulla, *Mater. Lett.*, 2008, **62**, 4328–4331.
30 Z. L. Wang and Z. W. Pan, *Adv. Mater.*, 2002, **14**, 1029–1032.
31 N. V. Hieua, N. A. P. Duc, T. Trung, M. A. Tuan and N. D. Chien, *Sens. Actuators, B*, 2010, **144**, 450–456.
32 A. Jamal, M. M. Rahman, S. B. Khan, M. Faisal, K. Akhtar, M. A. Ru, A. M. Asiri and A. O. Al-Youbi, *Appl. Surf. Sci.*, 2012, **261**, 52–58.
33 H. G. Bonilla, J. R. Gomez, A. G. Bonilla, D. P. Zepeda, J. T. G. Bonilla, L. G. Ortiz and M. F. Martinez, *J. Chem. Chem. Eng.*, 2013, **7**, 395–401.
34 H. G. Bonilla, V. M. R. Betancourtt, J. T. G. Bonilla, J. R. Gómez, L. G. Ortiz, M. F. Martínez, M. L. O. Amador and J. S. Salazar, *J. Nanomater.*, 2015, **2015**, 979543.
35 J. Tamaki, Y. Yamada, Y. Yamamoto, M. Matsuoka and I. Ota, *Sens. Actuators, B*, 2000, **66**, 70–73.
36 B. L. Zhu, C. S. Xie, A. H. Wang, D. W. Zeng, M. L. Hu and W. Y. Wang, *Mater. Res. Bull.*, 2004, **39**, 409–415.
37 H. G. Bonilla, V. M. R. Betancourtt, J. T. G. Bonilla, L. G. Ortiz, A. G. Bonilla, Y. L. C. Moreno, O. B. Alonso and J. R. Gomez, *Sensors*, 2018, **18**, 2299–2315.
38 A. G. Bonilla, O. B. Alonso, J. T. G. Bonilla, M. L. O. Amador, V. M. R. Betancourtt, A. S. Martínez, J. P. M. Lázaro, M. M. García and H. G. Bonilla, *J. Mater. Sci.: Mater. Electron.*, 2018, **29**, 15632–15642.
39 H. G. Bonilla, L. G. Ortiz, M. O. Amador, J. S. Salazar, V. M. R. Betancourtt, A. G. Bonilla and J. R. Gomez, *J. Nanomater.*, 2015, **2015**, 308465.
40 A. Singh, A. Singh, S. Singh and P. Tandon, *Chem. Phys. Lett.*, 2016, **646**, 41–46.
41 V. M. R. Betancourtt, H. G. Bonilla, M. F. Martínez, A. G. Bonilla, J. P. M. Lazaro, J. T. G. Bonilla, M. A. Gonzalez and M. L. O. Amador, *J. Nanomater.*, 2017, **2017**, 1–9.
42 H. G. Bonilla, M. F. Martinez, V. M. R. Betancourtt, A. G. Bonilla, J. R. Gomez, L. G. Ortiz, M. L. O. Amador and J. S. Salazar, *Sensors*, 2016, **16**, 177.
43 D. Larcher, A. S. Prakash, L. Laffont, M. Womes, J. C. Jumas, J. Olivier-Fourcade, M. S. Hedge and J. M. Tarascon, *J. Electrochem. Soc.*, 2006, **153**, A1778–A1787.
44 D. P. Dutta, A. Ballal, A. Singh, M. H. Fulekar and A. K. Tyagi, *Dalton Trans.*, 2013, **42**, 16887–16897.

45 N. Arunkumar and R. Vijayaraghavan, *RSC Adv.*, 2014, **4**, 65223–65231.
46 W. Liu, P. Lin, H. Jin, H. Xue, Y. Zhang and Z. Li, *J. Mol. Catal. A: Chem.*, 2011, **349**, 80–85.
47 J. Singh, N. Bhardwaj and S. Uma, *Bull. Mater. Sci.*, 2013, **36**, 287–291.
48 M. K. Balasubramaniam and S. Balakumar, *Chem. Pap.*, 2020, **74**, 55–75.
49 M. Balasubramaniam and S. Balakumar, *New J. Chem.*, 2018, **42**, 6613–6616.
50 M. Balasubramaniam and S. Balakumar, *Mater. Chem. Phys.*, 2019, **224**, 334–348.
51 M. Balasubramaniam and S. Balakumar, *Mater. Sci. Semicond. Process.*, 2016, **56**, 287–294.
52 J. Li, D. Ke, Y. Lai, Y. Chen and Z. Zhang, *J. Mater. Chem. A*, 2017, **5**, 10843–10848.
53 S. Goutham, N. Jayarambabu, C. Sandeep, K. K. Sadasivuni, D. S. Kumar and K. V. Rao, *Microchim. Acta*, 2019, **6**, 861–869.
54 B. G. Ghule, S. F. Shaikh, N. M. Shinde, S. S. Sangale, P. V. Shinde and R. S. Mane, *Mater. Res. Express*, 2018, **5**, 125001.
55 S. Thakur and P. Patil, *RSC Adv.*, 2016, **6**, 45768–45782.
56 D. Zhang, G. Dong, Z. Wu, W. Pan and X. Fan, *IEEE Sens. J.*, 2019, **19**, 2855–2862.
57 B. Chaitongrat and S. Chaisitsak, *J. Nanomater.*, 2018, **2018**, 9236450.
58 N. Saxena, P. Kumar and V. Gupta, *Nanoscale Adv.*, 2019, **1**, 2382–2391.
59 S. Singh, V. Gupta, B. C. Yadav, P. Tandon and A. K. Singh, *Sens. Actuators, B*, 2014, **195**, 373–381.
60 W. Z. Wang, G. H. Wang, X. S. Wang, Y. J. Zhan, Y. K. Liu and C. L. Zheng, *Adv. Mater.*, 2002, **14**, 67–69.
61 A. K. Jaiswal, S. Singh, A. Singh, R. R. Yadav, P. Tandon and B. C. Yadav, *Mater. Chem. Phys.*, 2015, **154**, 16–21.
62 D. A. Pomogailo, S. Singh, M. Singh, B. C. Yadav, P. Tandon, S. I. Pomogailo, G. I. Dzhardimalieva and K. A. Kydralieva, *Inorg. Mater.*, 2014, **50**, 296–305.
63 Z. Li, H. Li, Z. Wu, M. Wang, J. Luo, H. Torun, *et al.*, *Mater. Horiz.*, 2019, **6**, 470–506.
64 A. Singh, A. Singh, S. Singh and P. Tandon, *Sens. Actuators, B*, 2017, **244**, 806–814.
65 N. B. Tanvir, C. Wilbertz, S. Steinhauer, A. Kock, G. Urban and O. Yurchenko, *Mater. Today: Proc.*, 2015, **2**, 4190–4195.
66 F. R. Juang, *IEEE Sens. J.*, 2019, **19**, 4381–4385.
67 P. Viswanathan, A. K. Patel, J. Pawar, A. Patwardhan and R. Henry, *IETE J. Res.*, 2018, DOI: 10.1080/03772063.2018.1502625.
68 N. V. Hieu, N. D. Khoang, D. D. Trung, L. D. Toan, N. V. Duy and N. D. Hoa, *J. Hazard. Mater.*, 2013, **244**, 209–216.
69 T. Krishnakumar, R. Jayaprakash, T. Prakash, D. Sathyaraj, N. Donato, S. Licoccia, M. Latino, A. Stassi and G. Neri, *Nanotech*, 2011, **22**, 325501.
70 H. J. Yoon, D. H. Jun, J. H. Yang, Z. X. Zhou, S. S. Yang and M. M. C. Cheng, *Sens. Actuators, B*, 2011, **157**, 310–313.
71 D. Wang, Y. Chen, Z. Liu, L. Li, C. Shi, H. Qin and J. Hu, *Sens. Actuators, B*, 2016, **227**, 73–84.
72 N. B. Tanvir, O. Yurchenko, C. Wilbertz and G. Urban, *J. Mater. Chem. A*, 2016, **4**, 5294–5302.